In-Process Monitoring of Porosity in Additive Manufacturing using Optical Emission Spectroscopy

Mohammad Montazeri[1], Abdalla R. Nassar[2,3], Alexander J. Dunbar[2], Prahalada Rao[1*].

[1] Department of Mechanical and Materials Engineering, University of Nebraska-Lincoln, 68516
[2] Applied Research Laboratory, Pennsylvania State University, 18602
[3] Department of Engineering Science and Mechanics, Pennsylvania State University, 18602

Abstract

A key challenge in metal additive manufacturing is the prevalence of defects, such as discontinuities within the part (e.g., porosity). The objective of this work is to monitor porosity in laser powder bed fusion (L-PBF) additive manufacturing of nickel alloy 718 (popularly called Inconel 718) test parts using in-process optical emission spectroscopy. To realize this objective, cylinder-shaped test parts are built under different processing conditions on a commercial L-PBF machine instrumented with an in-situ multispectral photodetector sensor. Optical emission signatures are captured continuously during the build by the multispectral sensor. Following processing, the porosity-level within each layer of a test part is quantified using X-ray computed tomography (CT). The graph Fourier transform coefficients are derived layer-by-layer from signatures acquired from the multispectral photodetector sensor. These graph Fourier transform coefficients are subsequently invoked as input features within various machine learning models to predict the percentage porosity-level in each layer with CT data taken as ground truth. This approach is found to predict the porosity on a layer-by-layer basis with an accuracy of ~90% (F-score) in a computation time less than 0.5 seconds. In comparison, statistical moments, such as mean, variation, etc., are less accurate (F-score ≈ 80%) and require a computation time exceeding 5 seconds.

Key Words: Additive Manufacturing, Laser Powder Bed Fusion, In-Process Monitoring, Porosity, Optical Emission Spectroscopy, Photodetector, Inconel 718, Spectral Graph Theory, Graph Fourier Transform, X-Ray Computed Tomography, Machine Learning.

*corresponding author: rao@unl.edu

1 Introduction

1.1 Background and Motivation

The goal of this work is the identification and isolation of defects, such as porosity, in laser powder bed fusion (L-PBF) additive manufacturing using in-process sensor data. In L-PBF, material in the form of powder is rolled or raked across a build plate. The part is formed by selectively melting areas of the powder, layer-by-layer, using a laser (Gibson, Rosen *et al.* 2010, Sames, List *et al.* 2016). The laser position is controlled using a galvanometric mirror assembly. The focusing optic (typically) is a f-theta lens that maintains a stable diameter and focus of the laser beam on the build plate.

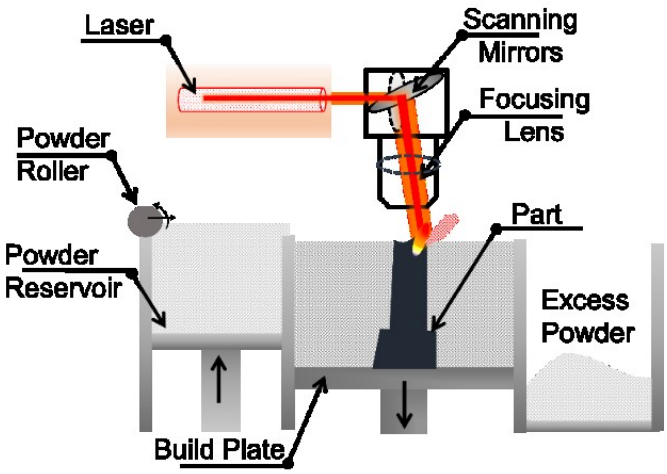

Figure 1: A schematic of the laser powder bed fusion (L-PBF) additive manufacturing process.

Despite the demonstrated potential of laser powder bed fusion (L-PBF) to revolutionize manufacturing, process repeatability, and part consistency remain open challenges (2013, Huang, Leu *et al.* 2015). Defects in L-PBF are diverse and result from complex, poorly understood interactions amongst process phenomena, materials, processing conditions, and machine dynamics (Grasso and Colosimo 2017). Although the critical process parameters, such as laser power (P, W), hatch spacing (H, mm), scan velocity (V, mm/s), and layer height (mm) can be optimized for certain part geometries, and aggregated in terms of the global volumetric energy density ($E_V = \frac{P}{V \times H \times T}$ J/mm^3), part defects can still occur (Olakanmi, Cochrane *et al.* 2015, Yusuf and Gao 2017).

In part, this is because the global energy density does not account for the magnitude and direction of the heat flow in the part (heat flux), which may change depending on the part geometry, orientation, and its location on the build plate (Yavari, Cole *et al.* 2019). Nor does energy density account for the subtle machine-related malfunctions and random flaws.

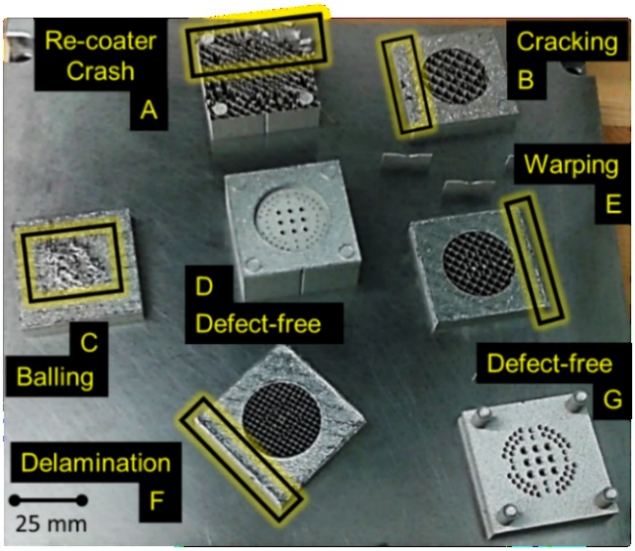

Figure 2: In L-PBF part quality tends to be inconsistent, for instance, out of the seven different orientations of the same part geometry built under identical process conditions, only two (part D and part G) were completed without any visible defects.

The quality assurance-related challenges in L-PBF are exemplified in Figure 2, which shows seven identical parts built simultaneously on a commercial L-PBF machine by the authors. The parts vary only in their build orientation; all other process conditions are identical. Notwithstanding, extensive process automation, and besides using the default process parameters settings for the material recommended by the machine manufacturer, only two parts out of seven were built successfully. The rest of the five builds were afflicted with various other types of defects, which renders them unfit for operational use. Such low process reliability makes L-PBF difficult to scale commercially (Lewandowski and Seifi 2016, Mazumder 2015, Seifi, Gorelik *et al.* 2017).

Due to the high-probability of defects occurring within L-PBF components, quality inspection of components for aerospace and defense applications using X-Ray Computed Tomography (CT) is the norm. Unfortunately, CT is expensive, and its resolution progressively degrades with increasing part size and

density (Seifi, Gorelik *et al.* 2017). Detection of defects during part production using in-process monitoring may thus provide a less expensive and more scalable approach for part certification.

One such strategy is to build a library of sensor signatures corresponding to specific defects for representative parts. Subsequently, this library can be used for rapid qualification of part quality (Lewandowski and Seifi 2016, Mazumder 2015, Seifi, Gorelik *et al.* 2017). If such a strategy for the in-process qualification of part quality is successful, it will lead to a *qualify-as-you-build* paradigm in AM, thus expanding the reach of AM to strategically important sectors (Mies, Marsden *et al.* 2016, Peralta, Enright *et al.* 2016).

1.2 Objective and Hypothesis

The objective of this work is to predict the presence and level or severity of porosity in LPBF parts using in-process optical emission spectroscopy signatures. To realize this objective, first, the line-to-continuum ratio of chromium emission around 520 nm are monitored during L-PBF of nickel alloy 718 (UNS N07718, popularly called Inconel 718) powder feedstock (Dunbar and Nassar 2018). Next, we develop and apply a graph theoretic approach to analyze the acquired line-to-continuum optical emission signatures.

The graph theoretic approach transforms the line-to-continuum measurements into features called graph Fourier transform coefficients. These graph Fourier transform coefficients are subsequently used as derived process signatures to predict the presence and level of porosity, layer-by-layer, using machine learning models. The correlation between the predicted and actual level of porosity is verified via offline CT of the parts. Accordingly, the underlying hypothesis is that the graph Fourier transform coefficients extracted from the in-process optical spectroscopy signatures are capable of discriminating the level of porosity in L-PBF parts with a higher fidelity compared to conventional statistical features, such as mean and standard deviation extracted from the optical emission spectroscopy signal.

Graph theoretic approaches have been used in our prior work for monitoring of process anomalies in L-PBF, such as detecting aberrations in the meltpool behavior from thermal imaging data (Montazeri and

Rao 2018). However, this work uses a different graph theoretic approach, based on the concept of graph Fourier coefficients to detect porosity in a layer-by-layer manner from data obtained from optical emission signals. In other words, the experimental data, type of defect monitored, sensor signatures obtained, and analytical approach used differ significantly from our previous studies and represent a novel approach for identification of L-PBF defects using in-situ sensor data.

The rest of this paper is organized as follows. A review of the literature, focused on optical spectroscopy monitoring in metal AM, is provided in Section 2. In Section 3, we describe the research methodology and explain the graph theoretic technique used to analyze the data. This is followed by discussion of the results and conclusions in Sections 4 and 5, respectively.

2 Literature Review

Several comprehensive review articles have been recently published describing sensing techniques for process monitoring in metal AM processes (Everton, Hirsch *et al.* 2016, Foster, Reutzel *et al.* 2015, Grasso and Colosimo 2017, Mani, Lane *et al.* 2017, Sharrat 2015, Spears and Gold 2016, Tapia and Elwany 2014). Here, we primarily focus on optical emission-based techniques utilizing single-point photodetectors (e.g. photodiode and spectrometers). While imaging sensors, such as infrared and optical cameras are capable of providing spatially-resolved data indicative of build quality (Gobert, Reutzel *et al.* 2018, Jacobsmuhlen, Kleszczynski *et al.* 2013, Khanzadeh, Chowdhury *et al.* 2017, Krauss, Eschey *et al.* 2012, Lane, Lane *et al.* 2016, Lane, Whitenton *et al.* 2016, Mahmoudi, Ezzat *et al.* 2019), an advantage of single-point photodetectors is their fast response rates (sampling rates exceeding 100 kHz are possible) and relatively low cost (Song, Bagavath-Singh *et al.* 2012).

The early use of photodetector for process monitoring has been exemplified largely in the context of the directed energy deposition (DED) metal AM process, hence this review cites articles from the DED perspective. Mazumder *et al.* have pioneered the use of photodetectors for closed-loop control in metal DED (Mazumder, Dutta *et al.* 2000, Mazumder and Song 2016, Mazumder, Song *et al.* 2017, Song and Mazumder 2011, Song and Mazumder 2015). One of their early works describes the use of three

photodetectors for closed-loop control of the surface finish, geometry, and microstructure of the part by modulating the energy density via changes in the build height (Mazumder, Dutta *et al.* 2000). As a result of this closed-loop control strategy, the surface roughness improved by as much as 20%, and parts with unusual bulk properties, such as negative coefficient of thermal expansion, were produced. Recent patents by Mazumder *et al.* also describe the use of optical spectrometery-based closed-loop control in DED (Mazumder and Song 2016, Mazumder, Song *et al.* 2017). Through various examples, including DED of titanium and Nickel-based superalloys, Muzumder *et al.* show that the intensity of the optical spectroscopy line emissions correlate with phase transformation in the material, this relationship is further extended for prediction of the microstructure of the resulting material.

Spectroscopy has also been investigated for detection of defects and undesirable process conditions, such as lack of deposition and overbuilding in DED. For example, Mazumder *et al.* have proposed a *smart additive manufacturing system* wherein emission are used as an input into a closed-loop control schema for processing parameters (e.g. laser power, beam spot size) to tailoring the microstructure (Mazumder and Song 2016). In a similar vein, Nassar *et al.* have demonstrated a correlation between the line-to-continuum ratios around specific spectral emission wavelengths during DED of Ti-6Al-4V titanium alloys and the occurrence of lack-of-fusion defects (Stutzman, Nassar *et al.* 2018). They isolated lack-of-fusion in Ti-6Al-4V using optical emissions spectroscopy around 430 nm and 520 nm wavelength, as well as using an optical camera filtered around 430 nm. More recently, spectroscopy has been applied to the L-PBF process by Dunbar and Nassar and optical emissions have been demonstrated to correlate to processing conditions and part porosity (Dunbar and Nassar 2018). Here, we build on the work of Dunbar and Nassar by developing and applying spectral graph theory together with machine learning to predict the presence and level or severity of porosity using in-process optical emission spectroscopy signatures in L-PBF.

From a data analytics perspective, machine learning approaches using in-process sensor data are being intensively applied in AM for defect detection (Grasso and Colosimo 2017). For instance, neural networks are trained (both unsupervised and supervised learning) to recognize patterns from in-situ sensors, such as

meltpool shape and size, and these patterns are correlated with defect severity based on offline characterization of the part quality, typically with X-ray computed tomography (Grasso, Laguzza *et al.* 2016, Imani, Gaikwad *et al.* 2018, Imani, Gaikwad *et al.* 2018, Khanzadeh, Chowdhury *et al.* 2017, Montazeri and Rao 2018, Montazeri, Yavari *et al.* 2018, Repossini, Laguzza *et al.* 2017, Tapia, Elwany *et al.* 2016, Williams, Dryburgh *et al.* 2018). However, using machine learning is fraught with two major drawbacks.

First, generalizability of machine learning models remains poor, because, supervised machine learning models are trained on labeled outputs, typically CT scans, pertaining to a specific part geometry and sensor data stream to detect one type of defect. Therefore, they have to be re-trained for new parts because each new geometry and process condition will impose a unique signal pattern. Second, obtaining a large labeled set of data for machine learning is not viable in AM due to the slow process speed, small batch sizes, expensive consumables, and time required for sample characterization. Lastly, machine learning algorithms have been trained to detect part defects in rudimentary geometries, such as thin-walls, cylinders and cubes. The validity of the machine learning algorithms to detect defects in the AM of complex freeform geometries is still in its infancy (Abdelrahman, Reutzel *et al.* 2017).

We acknowledge that some of these drawbacks inherent to machine learning are shared by the graph theory approach presented in this work. Two particular drawbacks stand out. First, the line-to-continuum ratio measured in this work is specific to Chromium emissions in Inconel 718, hence, the sensing system will have to be adjusted accordingly when a different material is used – this is rather tractable as only two optical filters have to be replaced. The proposed method is also a supervised learning approach which relies on *a priori* labeled CT data, and is geared towards detection of one type of defect, namely, lack-of-fusion porosity.

In closing this section, we note that direct observation of porosity from sensor data without the need for intervening machine learning techniques remains an active research challenge. This is because porosity occurs in the range of 10 μm to 100 μm, with pinhole-type porosity at the lower end, and lack-of-fusion

porosity in the higher range (Maskery, Aboulkhair *et al.* 2016). To capture porosity at the part-level would require the thermal or optical sensor to have commensurate resolution, while at the same time have a large enough field-of-view. Recently, researchers at Lawrence Livermore National Laboratories have demonstrated the use of in-situ synchrotron X-Ray imaging for detection of keyhole porosity (Calta, Wang *et al.* 2018). This instrument tracks the meltpool at frame rates of 4 kHz. However, the scale of the substrate on which the instrument capabilities are demonstrated is approximately 2 mm. The recent advancement of a new in-process sensing approach called Spatially Resolved Acoustic Spectroscopy (SRAS) pioneered by the research group in Nottingham University UK by Smith *et al.* and Clare *et al.* presents a viable opportunity for direct visualization of porosity in larger samples (Smith, Li *et al.* 2014, Williams, Dryburgh *et al.* 2018).

3 Methods

3.1 Sensor Data Collection

Part Build Conditions

Cylindrical test parts (discs) are built simultaneously on a 3D Systems ProX DMP 200 L-PBF machine. Each disc is 12 mm in diameter and 6.6 mm in height. The build direction is parallel to the vertical axis of each cylinder. Laser power (P, W), laser scan velocity (V, mm/s), and hatch spacing (H, mm) are varied for each disk. Four discs, labeled A through D, are selected for analysis — processing parameters for these discs are noted in Figure 3. The layer thickness is held constant at ≈ 30 μm. We note that the intent of these experiments is not to conduct a parameter optimization study, but rather to generate distinct levels of pore severity within the samples.

Sensor Instrumentation and Operating Principle

The ProX 200 machine is equipped with a photodetector-based sensor, i.e. multispectral sensor, detailed in Ref. (Dunbar and Nassar 2018, Stutzman, Nassar *et al.* 2018). As shown in Figure 4, the sensor array consisted of two off-axis photodetectors (photodiodes) that capture light from the laser-material interaction zone. A custom optical system is used to image the build plate of the L-PBF machine (140 mm

× 140 mm) onto the sensor of each photodiode. Bandpass optical filters are used to capture emissions around 520 nm and 530 nm (10 nm FWHM) —this approach is detailed in the authors previous works (Dunbar and Nassar 2018, Nassar, Spurgeon *et al.* 2014, Stutzman, Nassar *et al.* 2018). The output current of each photodetector is amplified and converted to a voltage, which is sampled at 100 kHz.

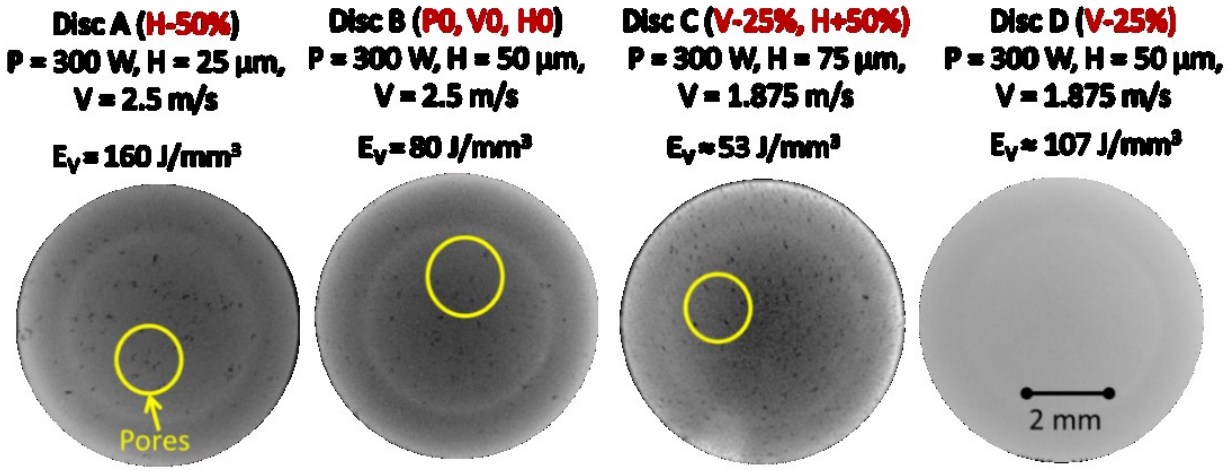

Figure 3: The four discs used for analysis in this work made by varying the power (P), velocity (V), and hatch spacing (H) settings.

Photodetector outputs are synchronized with the laser scanner position, laser trigger, and laser power output. Hence, the part geometry and scan pattern are matched one-to-one. The NIST atomic spectra database is used as the reference for selecting the line and continuum wavelengths (Kramida, Ralchenko *et al.* 2017). Nassar *et al.* in a series of publications have explained implementation details and the physical meaning of the line to continuum ratio – i.e., the relationship of the line-to-continuum emission to the elemental excitation of alloy constituents of the powder feedstock, and through it to the quality of the build (Dunbar and Nassar 2018, Nassar, Starr *et al.* 2015, Stutzman, Nassar *et al.* 2018).

Key details are reiterated here for the convenience of the reader. The multispectral sensor is designed to measure the line-to-continuum ratio of chromium emission (Cr I) (Nassar, Starr *et al.* 2015). Chromium makes up 17-21%, by mass, of the composition of nickel alloy 718, and exhibits strong, atomically-excited emission lines around 520 nm. Continuum emissions of the plume, meltpool, including blackbody radiations and other extraneous sources are accounted for by measuring emission around 530 nm. The underlying principle is illustrated in Figure 5.

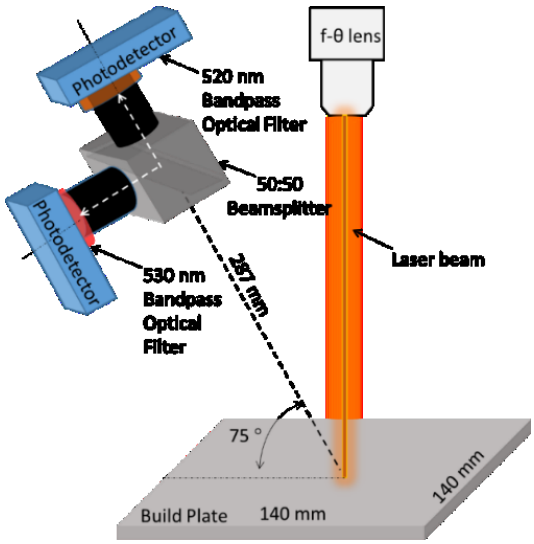

Figure 4: Schematic of the multispectral sensor installed within the AM machine.

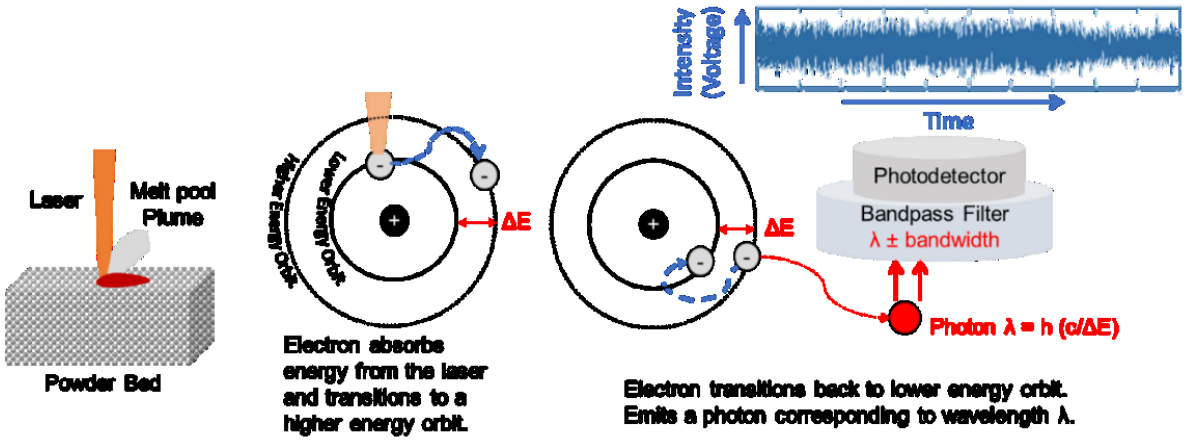

Figure 5: The operating principle of the multispectral sensing system used in this work.

The line-to-continuum ratio is described in Eq. (1), where S_{Line} is the sum (integration) of spectral line emission amplitudes in the 520 nm ± 5 nm band, and $S_{Continuum}$ is the amplitude of the continuum emission summed under the 530 nm ± 5 nm wavelength region. Nassar *et al.* (Dunbar and Nassar 2018, Nassar, Spurgeon *et al.* 2014, Stutzman, Nassar *et al.* 2018) have shown that the numerator term, $S_{Line} - S_{Continuum}$, in Eqn. (1) ensures that the part of the frequency spectrum corresponding to the extraneous noise is suppressed.

$$S_{Line-to-Continuum} = \frac{S_{Line} - S_{Continuum}}{S_{Continuum}} \quad (1)$$

3.2 Porosity Measurement

The parts are characterized post-process using X-Ray Computed Tomography (CT); Figure 6 exemplifies a representative. CT is selected over other density measurement techniques because it provides a layer-by-layer measurement of the distribution, size and type of defects in the part in a non-destructive manner (Slotwinski, Garboczi *et al.* 2014, Spierings, Schneider *et al.* 2011). This enables calculation of porosity on a layer-by-layer basis, which is not possible with measurements of bulk density (e.g. Archimedes density).

CT of the four discs is carried out on a GE Phoenix *v|tome|x m* system using a beam voltage of 170 kV and a voxel resolution of 0.015 mm (15 μm). Porosity information is extracted using three image processing steps to detect the boundary of each pore and label its interior:

1. The boundary of each disc is identified cropped and the brightness and contrast of the CT slice is enhanced using heuristically-selected values for each disk (Figure 6(b)).
2. Canny edge detection is used to identify edges of pores and the image is binarized (Figure 6(c)) (Canny 1987).
3. This is followed by iterative image dilation and segmentation of pores (pixel value=1) from dense material (pixel value=0) (Figure 6(d)). Note that some of the smallest pores, were identified as dense material, however this appeared consistent across all disks.

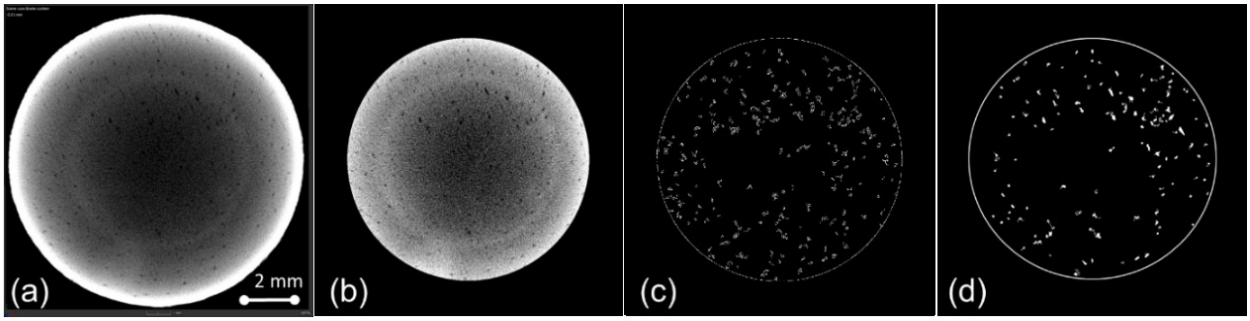

Figure 6: Image processing steps to extract the porosity from CT slices for layer 18 Disc C with (a)the original unprocessed CT slice, (b) the cropped image after image enhancement, (c) the detected edges located around the pores and disc cross section in a binary format, and (d) the dilated edges that are filled with pixel values equal to 1 to construct the whole pores in a layer of the disc.

Porosity Quantification.

From the binary image from Figure 6(d), we extract the following metrics to characterize porosity as functions of build layer:

i. The proportion of area in a layer affected by porosity (ρ_1),

ii. Frequency of occurrence, i.e., number of discrete pores in a layer (ρ_2),

iii. The average distance between a pair of pores (ρ_3), and

iv. Finally, the above three metrics are combined into a single metric, called the normalized porosity level (μ).

The proportion of area covered by pores in a layer (ρ_1, unitless) defines the ratio of the pore pixels divided by all pixels on a layer. If the binary image of a layer is represented as a matrix with M rows and N columns, with each element (pixel) $p_{i,j}$ then,

$$\rho_1(layer) = \frac{\text{Pixels related to the pores}}{\text{All pixels in the image}} = \frac{\sum_{i=1}^{i=M}\sum_{j=1}^{j=N} p_{i,j}}{\text{M} \times \text{N}} \quad (2)$$

The number of the pores in a layer (ρ_2, unitless) is defined as the number of pores in a layer. This is found by counting the number of distinct pore centroids on each layer. If the centroids are marked as $c_1 \dots c_k$, then ρ_2 is given as,

$$\rho_2(layer) = |c_i|_0 \ \forall i; \ \ i = \{1 \dots k\} \quad (3)$$

The average distance between pores in a layer (ρ_3, pixels) is the mean pairwise distances between the centroid of the pores. The numerator in Eq. (3) is the sum of the Euclidean distance between pores, and the denominator is the number of pairs of pores.

$$\rho_3(layer) = \frac{\sum_{\forall i,j}\left\|c_i - c_j\right\|_2}{\binom{\rho_2}{2}}\,[\text{pixles}] \ \ \forall i,j; i,j = \{1 \dots k\} \quad (4)$$

The normalized porosity level (μ, unitless) combines ρ_1, ρ_2, and ρ_3 into a dimensionless number (μ) between 0 and 1. We assume that ρ_1, ρ_2, and ρ_3 are all non-zero. According, μ is obtained in two steps, first, in Eq. (5) the porosity measure ρ_4 is obtained for each layer. Subsequently, the ρ_4 value is normalized, in Eq. (6) to obtain a value between 0 and 1.

$$\rho_4(layer) = \frac{\rho_1 \times \mathrm{M} \times \mathrm{N}}{\rho_2 \times \rho_3} \frac{[\mathrm{pixles}^2]}{[\mathrm{pixles}]} = \frac{\sum_{i=1}^{i=M} \sum_{j=1}^{j=N} p_{i,j}}{\rho_2 \times \rho_3} [\mathrm{pixles}] \quad (5)$$

$$\mu(layer) = \frac{\rho_4 - \min(\rho_4)}{\max(\rho_4) - \min(\rho_4)} \quad (6)$$

The metric μ is thus a normalized value whose physical significance can be explained as follows. The area occupied by pores in a layer is represented in ρ_1, hence a small ρ_1 is desirable for a fully-dense component. However, ρ_1 does not capture how many pores account for this area. For example, one big pore of a certain area *A* may have a more deleterious effect on the physical properties of the part than multiple pores which add up to the same area *A*, i.e., the smaller the ratio ρ_1/ρ_2 the better, at least in terms of fatigue properties (Yadollahi, Mahtabi *et al.* 2018). Next, having pores farther away from each other is more desirable than having two pores closer together. Hence, the average distance between the pores (ρ_3) should also be taken into account with the physical contention that the severity of porosity is inversely proportional to ρ_3. We note that if ρ_1 is zero for a layer, such as in Disc D, the number μ is forced to zero, representing a fully dense layer.

In Sec. 4, we will use these quantifiers of porosity, namely, ρ_1 , ρ_2, ρ_3 and μ, as the response (output) to be predicted for each layer as a function of graph theoretic Laplacian Eigenvectors and Eigenvalues extracted from the multispectral sensor data. The procedure to derive these graph theoretic process signatures is described in the forthcoming section, Sec. 3.3.

3.3 Extraction of Graph Fourier Transform Features from Sensor Data

Graph Fourier transform coefficients are extracted from the line-to-continuum signatures and used to predict the pore severity in each layer. The mathematical underpinnings of the methodology have been addressed in the authors' previous work, we have restated some of it here for the sake of continuity (Montazeri and Rao 2018, Montazeri, Yavari *et al.* 2018). Detailed mathematical justifications for the approach are available in Ref. (Montazeri and Rao 2018, Tootooni, Rao *et al.* 2018). In the previous works we mainly correlated the sensor signatures with defects due to overhang and contamination in LPBF, these are described in Ref. (Montazeri and Rao 2018), and Ref. (Montazeri, Yavari *et al.* 2018), respectively.

Graph theoretic approaches have also been used in the context of surface finish assessment in semiconductor nanomanufacturing and machining (Rao, Beyca *et al.* 2015, Tootooni, Liu *et al.* 2016). This work builds on the prior publications but is novel because, for the first time, sensor data are reconstructed into undirected weighted graphs to extract the graph Fourier coefficients for each layer. These graph Fourier coefficients are then used to predict the level of porosity in each layer.

Step 1: Transforming the one-dimensional multi-spectral signal into a graph.

In this step, the aim is to convert the one-dimensional line-to-continuum ratio signatures into a weighted, undirected graph $G(V, E, W)$. Where V, E and W are the vertices, edges and weight between the edges, of a network graph, respectively. To begin with the graph conversion process, the multi-spectral data for each layer of a disc (approximately 56,000 to 157,000 points) are represented as a signal matrix ($\boldsymbol{X}_l$), where l is the layer number. The number of data points per layer depends upon the scan velocity and hatch spacing – a higher scan speed and greater hatch spacing results in fewer data points given the constant data acquisition rate of 100 kHz. The total number of data points per layer for each disc is detailed in Table 1.

Line-to-continuum data, synchronized with scanner position and system time, are available for 110 layers for each disc, i.e., l = 1, 2, …, 110 indexed. For each layer of each disk, data are separated into windows of 50 data points, which corresponds to approximately 1 mm and 1.25 mm of scan length for the lowest (1.875 m/sec, Discs C and D) and highest scan velocity (2.5 m/sec, Discs A and B), respectively. The approach is illustrated in Figure 7.

Based on extensive offline studies, summarized in Appendix I, the window size of 50 data points was found to be the smallest possible window found to have the highest statistical fidelity. This windowing approach allows the signal to be converted into a matrix with a fixed number of columns. That is, each row of the matrix $\boldsymbol{X}_l$ is a 50 data point signal segment of a layer (l). The window size is the only heuristic parameter used in the approach. The matrix $\boldsymbol{X}_l$ thus has N rows and d (=50) columns. The value number of rows, N, varies between ~3100 to ~1100 and is inversely proportional to the laser velocity and hatch spacing (Table 1).

Table 1: Approximate number of data points available per layer for a particular disc, and the corresponding number of rows (N) for each layer (d = 50).

Discs	mean and standard deviation of the line-to-continuum ratio	Average number of line-to-continuum ratio data points per layer	Number of rows (N) in the signal matrix $\boldsymbol{X_l}$ with window size of 50 data poins.
Disc A	18.6 (4.5)	157000	3140
Disc B	4.0 (0.9)	76000	1620
Disc C	4.9 (0.4)	56000	1120
Disc D	10.3 (0.8)	113000	2260

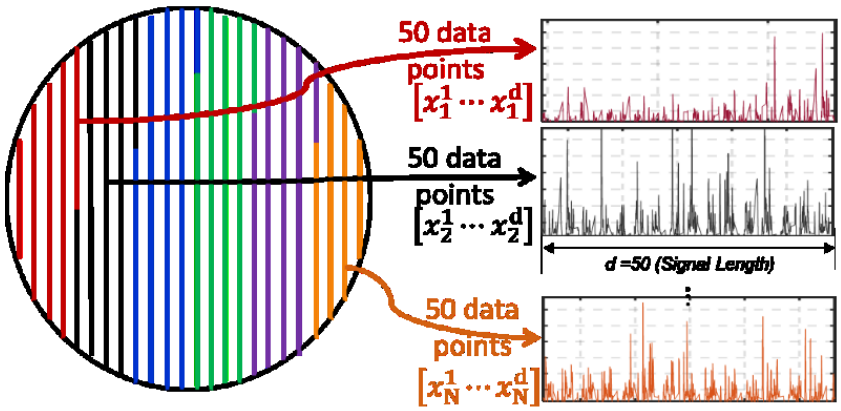

Figure 7: Illustration of the approach taken to window the signal in each layer into 50 data point long segments. The diagram is not to scale.

The signal matrix ($\boldsymbol{X}_l$) is setup for each layer as follows,

$$\boldsymbol{X}_l = \begin{bmatrix} x_1^1 & \cdots & x_1^d \\ \vdots & \ddots & \vdots \\ x_N^1 & \cdots & x_N^d \end{bmatrix} \forall l = \{l = 1,2,\ldots,L = 110\}, \text{and } d = 50. \quad (7)$$

Next, a pairwise comparison is made between each of the rows of the matrix $\boldsymbol{X}_l$. Such a pairwise comparison implies that the change in the signal across a layer is tracked, and each of the N rows in $\boldsymbol{X}_l$ becomes a node or vertex in the graph. The weight of an edge connecting one node (q) to another (r) in the graph is the pairwise distance between them. The distance w_{qr} is computed using a normed kernel function Ω per Eqn. (8), the kernel function can relate to a similarity measure, such as a Euclidean distance, between the set of data points in row r and q of the matrix $\boldsymbol{X}_l$. Thus if $\boldsymbol{x}^q$ and $\boldsymbol{x}^r$ are the q^{th} and r^{th} row vectors in $\boldsymbol{X}_l$, the similarity distance between them (w_{qr}) is written as,

$$w_{qr} = \Omega(\boldsymbol{x}^q, \boldsymbol{x}^r) \; \forall \; q, r \in (1 \cdots k). \quad (8)$$

Different types of kernel functions Ω can be selected,such as the radial basis or Euclidean kernel. In this work we use the Mahalanobis kernel shown in Eqn. (9) because it tends to normalize the data in matrix $\boldsymbol{X}_l$ with respect to its covariance $\boldsymbol{\Sigma}$.

$$\mathcal{w}_{qr} = (\boldsymbol{x}^q - \boldsymbol{x}^r)\boldsymbol{\Sigma}^{-1}(\boldsymbol{x}^q - \boldsymbol{x}^r) \tag{9}$$

Because, there are N rows in the matrix $\boldsymbol{X}_l$, we obtain a weighted undirected graph with N nodes and $\frac{N(N-1)}{2}$ edges. Once the pairwise distances $\mathcal{w}_{qr}$ are computed, they can be compacted into a *similarity matrix*. The similarity matrix $\boldsymbol{S_l}^{N\times N} = [\mathcal{w}_{qr}]$, which is symmetric, represents a weighted and undirected graph G. Hence, $\boldsymbol{S_l}$ is the matrix representation of the signal $\boldsymbol{X}_l$ in terms of the graph. Each row (or column) of $\boldsymbol{S_l}$ is a node in the graph. Each element is the weight of the edge connecting two nodes indexed by its row and column. For instance, the element $\boldsymbol{S_l}(i,j) = \boldsymbol{S_l}(j,i)$ represents the weight of the edge connecting node i and node j. In other words, the graph $G(V,E,W)$ is a lower dimensional, planar 2D graph representation of the relationship between each segment of the signal $\boldsymbol{X}_l$ in terms of the similarity matrix $\boldsymbol{S_l}$.

Step 2: Calculating the Eigen spectrum (topological information) of the graph

This step aims to extract topological information from the graph G by calculating the Laplacian Eigenvalues ($\boldsymbol{\Lambda}_l$) and Eigenvectors ($\boldsymbol{V}_l$), which are subsequently used to derive the graph Fourier transform coefficients. The graph Fourier transform coefficients are in turn used to predict the porosity-level (μ) in a layer. The normalized Laplacian matrix is first calculated in Eqn. (10) – Eqn. (12) based on the similarity matrix ($\boldsymbol{S}_l$) and degree matrix ($\boldsymbol{\mathcal{D}}_l$), where the degree matrix Eqn. (11) is the sum of each row in the similarity matrix. To be more specific, the degree of each node in the graph is described as the sum of weight of edges that are incident upon a node. In Eqn. (10), q represents a node on the graph.

$$d_q = \sum_{r=1}^{N} w_{qr} \;\; \forall\, q = \{1 \dots N\} \tag{10}$$

$$\boldsymbol{\mathcal{D}}_l \stackrel{\text{def}}{=} \text{diag}(d_1, \cdots, d_N). \tag{11}$$

Using the degree matrix, the normalized Laplacian $\boldsymbol{\mathcal{L}}$ of the graph G can be defined as,

$$\begin{gathered}\boldsymbol{\mathcal{L}}_l \stackrel{\text{def}}{=} {\boldsymbol{\mathcal{D}}_l}^{-\frac{1}{2}} \times (\boldsymbol{\mathcal{D}}_l - \boldsymbol{S}_l) \times {\boldsymbol{\mathcal{D}}_l}^{-\frac{1}{2}}, \\ \text{where, } {\boldsymbol{\mathcal{D}}_l}^{-\frac{1}{2}} = \text{diag}\left(1/\sqrt{d_1}, \cdots, 1/\sqrt{d_N}\right).\end{gathered} \tag{12}$$

Accordingly, the Eigen spectrum of $\boldsymbol{\mathcal{L}}$ is computed as,

$$\boldsymbol{\mathcal{L}}_l \boldsymbol{V}_l = \boldsymbol{\Lambda}_l \boldsymbol{V}_l. \tag{13}$$

And the graph Laplacian eigenvalues ($\boldsymbol{\Lambda}_l$) and Eigenvectors ($\boldsymbol{V}_l$) can be described as follows,

$$\begin{aligned} \boldsymbol{\Lambda}_l &= [\,\boldsymbol{\lambda}_{l,1};\ \boldsymbol{\lambda}_{l,2};\ \dots;\ \boldsymbol{\lambda}_{l,N}] \\ \boldsymbol{V}_l &= \left[[\boldsymbol{v}_{l,1}];[\boldsymbol{v}_{l,2}];\dots;[\boldsymbol{v}_{l,N}]\right] \end{aligned} \tag{14}$$

Where, $\boldsymbol{V}_l$ is composed of *N* individual Eigenvectors $\boldsymbol{v}_{l,(\cdot)}$, and $\boldsymbol{\Lambda}_l$ contains the corresponding number of Eigenvalues $\boldsymbol{\lambda}_{l,(\cdot)}$. All Eigenvalues are real and non-negative, and Eigenvectors are orthogonal to each other (because the matrix $\boldsymbol{\mathcal{L}}_l$ is symmetric and positive semi-definite). In other words, the Eigenvectors of the Laplacian matrix of a graph present an orthogonal basis, akin to a Fourier basis. These properties are encapsulated in Eqn. (15), with the caveat that the first Eigenvector is a unit vector ($\boldsymbol{v}_{l,1} = \vec{1}$) and the first Eigenvalue of $\boldsymbol{\mathcal{L}}_l$ is zero ($\boldsymbol{\lambda}_{l,1} = 0$).

$$\begin{gathered} \boldsymbol{v}_{l,2} \perp \boldsymbol{v}_{l,3} \perp \boldsymbol{v}_{l,i} \cdots \perp \boldsymbol{v}_{l,N}, \Rightarrow \langle \boldsymbol{v}_{l,i}, \boldsymbol{v}_{l,j} \rangle = 0 \ \forall i \neq j, \\ \text{and } \langle \boldsymbol{v}_{l,i}, \boldsymbol{v}_{l,j} \rangle = 1 \ \forall i = j, \text{ noting } \boldsymbol{v}_{l,1} = \vec{1} \\ \boldsymbol{\lambda}_{l,(\cdot)} \geq 0, \text{ and } \boldsymbol{\lambda}_{l,1} = 0 \end{gathered} \tag{15}$$

Step 3: Constructing the signal basis to obtain graph Fourier coefficients

In this step, the Eigenvectors $\boldsymbol{V}_l$ are used to transform a raw line-to-continuum signal into so-called graph Fourier coefficients. To realize this aim, a universal Eigenvector basis space is constructed. We frame a universal basis, ($\boldsymbol{\mathcal{V}}_{basis}$) as a time-weighted average of the Eigenvectors across layers for Disc D , which represents a prototype/ideal Eigenvector. This is necessary to account for noise and variance in Eigenvectors $\boldsymbol{V}_l$ across layers within each disk.

The procedure for obtaining the $\boldsymbol{\mathcal{V}}_{basis}$ is a layer-wise simple update schema. It is started with the Eigenvector of the first layer of ($\boldsymbol{V}_{l=1}$) of a disk. This Eigenvector are continually updated by a small portion ($\Delta < 0.01$) of the difference between the eigenvectors for the next consecutive layers for the disk, and so on. The procedure is mathematically represented as follows,

$$\begin{gathered} \boldsymbol{\mathcal{V}}_{l+1} = \boldsymbol{\mathcal{V}}_{\boldsymbol{l}} + \Delta\left(\boldsymbol{v}_{l+1,i} - \boldsymbol{v}_{l,i}\right), \forall\ l \in \{1 \dots L = 110\}, i \in \{1 \dots N\} \\ \boldsymbol{\mathcal{V}}_{basis} = \boldsymbol{\mathcal{V}}_L \end{gathered} \tag{16}$$

We define the spectral graph transform $\boldsymbol{C}$ using Eqn. (17), which is analogous to the discrete Fourier transform, as follows, where $\boldsymbol{X}_l$ is a sensor signal for a layer l which is a N data point long column vector (Shuman, Ricaud *et al.* 2012).

$$\boldsymbol{C} = [(\boldsymbol{X}_l)^T(\boldsymbol{\mathcal{V}}_{basis})] \tag{17}$$

As the $\boldsymbol{\mathcal{V}}_{basis}$ is fixed, using the above inner product through all the layers ($\boldsymbol{X}_l$) results in the graph coefficient matrix $\boldsymbol{C}$. The graph Fourier transform ($\boldsymbol{C}$) in this study is a $1\times N$ vector that results from the dot product of the $1 \times N$ line-to-continuum signals for each layer ($\boldsymbol{X}_l{}^T$) with the $N \times N$ dimensional Eigenvector basis ($\boldsymbol{\mathcal{V}}_{basis}$) (Sandryhaila and Moura 2013, Shuman, Narang *et al.* 2013, Shuman, Ricaud *et al.* 2012). However, to reduce the computational burden, we only use the first ten non-zero values of the $\boldsymbol{C}$ as input features for machine learning. Subsequent principal component analysis revealed that more than 85% of the variation in the dataset are captured within these first ten Eigenvectors in $\boldsymbol{\mathcal{V}}_{basis}$.

3.4 Predicting the porosity level using graph Fourier coefficients.

We use a two-fold strategy for predicting the porosity in a disc based on the coefficient matrix $\boldsymbol{C}$.

1) Classifying or binning the four porosity metrics, namely, proportion of area in a layer affected by porosity (ρ_1), Frequency of occurrence, i.e., number of discrete pores in a layer (ρ_2), average distance between a pair of pores (ρ_3), and normalized porosity level (μ) into discrete categories.
2) Estimating the value of the normalized porosity level (μ), instead of classifying into discrete levels.

The Eigenvectors basis ($\boldsymbol{\mathcal{V}}_{basis}$) are extracted from the nominally defect-free part, which in our case is Disc D. The Eigenvectors ($\boldsymbol{\mathcal{V}}_{basis}$) serve as basis or projection space for the sensor data. The key idea is explained as follows. When Fourier transform coefficients $\boldsymbol{C}$ belonging to nominal defect-free conditions, such as any layer of Disc D, are projected onto this space, they will cluster closely. Conversely, signals belonging to pore-afflicted layers will cluster away from the coefficients belonging to nominally porosity-free layers. The advantage of this approach is that the sensor data are transformed into a set of coefficients by obtaining a simple inner product multiplication (dot product) of the Laplacian Eigenvector with the signal of equal length as described in Eqn. (17).

Approach for classifying the normalized porosity level into discrete categories

We investigated a two-class (high and low) and three-class (high, medium, and low) classification of porosity level. Class groupings or labels are made per a threshold limit value of the various porosity metrics. The threshold values were selected so as to avoid highly unequal populations between classes and thus minimize the possibility of overfitting the data with machine learning models. Accordingly, we required each classes to have at least 100 corresponding measurements of a porosity-level.

For the two-class classification case, since μ ranges between [0,1], we set the threshold at 0.5. A normalized porosity level (μ) less than or equal to 0.5 for a layer is considered acceptable, while a value of μ over 0.5 is unacceptably high. In a similar vein, we demarcate $\rho_1 <$ 0.5% as acceptable-level, $\rho_1 \geq$ 0.5% as unacceptable–level; $\rho_2 <$ 30 as acceptable-level, $\rho_2 \geq$ 30 as unacceptable –level; $\rho_3 <$ 200 pixels as acceptable-level, $\rho_3 \geq$ 200 pixels as unacceptable-level.

For the three-class problem $\mu = 0$ is labeled as a low-level, $0 < \mu < 0.6$ is a medium-level, and $0.6 \leq \mu$ is a high-level. The three-levels for the other metrics are as follows: $\rho_1 \leq 0.5$ as low-level, $0.5 < \rho_1 \leq 1.2$ as medium-level, and $1.2 < \rho_1$ as high-level; $\rho_2 \leq 20$ as low-level, $20 < \rho_2 \leq 60$ as medium-level, and $60 < \rho_2$ as high-level; $\rho_3 \leq$ 200 pixels as low-level, 200 pixels $< \rho_3 \leq 240$ pixels as medium-level, and $240 < \rho_3$ pixels as high-level.

Six popular machine learning classification algorithms, namely, Support Vector Machine (SVM), Decision Tree (DT), K-Nearest Neighborhood (KNN), Linear Discriminant Analysis (LDA), K-Means, and a shallow Neural Network (NN) are used to classify the level of porosity. The aim of using six different algorithms is to show that irrespective of the machine learning approach used, the ability to accurately identify the level of porosity in a layer is higher with graph Fourier transform coefficients as features compared to statistical signal features.

In other words, we test the hypothesis that the graph Fourier transform coefficients extracted from the in-process spectral signatures are capable of discriminating the level of porosity in L-PBF parts with a higher statistical fidelity compared to conventional statistical signal features, such as mean and standard

deviation of the signal notwithstanding the type of modeling technique used. The fidelity of each input type is assessed based on the F-score, which is a combination of both Type I (false error) and Type II (failing to detect) statistical errors (Montazeri and Rao 2018). Extensive offline studies were done to optimize the parameters for these algorithms. The input features to the algorithms selected are one of the following two types, which correspond to 440 deposited layers (4 printed discs with 110 layers for each disc).

- Input Type 1: The graph Fourier coefficients ($\boldsymbol{C}$) obtained from the first ten non-zero Laplacian Eigenvectors ($\boldsymbol{V}_{basis}$) shown in Sec. 3.2, Eqn. (17).
- Input Type 2: Using five statistical features extracted from the line-to-continuum ratio, namely, the mean, standard deviation, range, skewness, kurtosis, interquartile range.

Each feature set is finally subjected to principal component analysis (PCA) to further compress the dimension of the data. This PCA-based dimension reduction transforms the features into orthogonal components. Further, to ensure equitable comparison between the input features, the number of principal components chosen corresponds to those capturing at least 85% of the variation in the data. Lastly, to keep the development tractable, we note that the graph theoretic Fourier transform coefficients are used as input features within a KNN model.

Training and testing are conducted using a 5-fold cross-validation procedure. The approach taken is as follows. For training, the dataset is split randomly into five groups with equal number of layers represented per group (110 layers per part = 440 layers for four part; 440/5 = 88 layers per group). Each of the algorithms studied is trained using data from the four groups; the training data set comprises 352 layers (4 groups for training × 88 layers per group = 352 layers for training). The trained model is then tested on the data from the fifth, i.e., the last remaining group (88 layers). This training-testing process is replicated five times, and then the average prediction fidelity in terms of the F-score obtained from the testing data set over these five repetitions are reported.

Estimating the normalized porosity value from in-situ data

We also use the in-process optical emission spectroscopy to predict the normalized porosity level, instead of classifying porosity values into discrete classes; the results are reported in Section 4. We implemented a simple feed-forward neural network with one hidden layers and ten neurons in the hidden layer designed to predict the exact porosity value (μ). In this neural network sigmoid activation functions are used in the hidden layer, and a linear activation function is used in the output layer. The backpropagation algorithm via Levenberg-Marquardt optimization is implemented to minimize the sum of squared error between the predicted ($\hat{\mu}_l$) and observed (μ_l) normalized porosity level over one layer (Demuth, Beale *et al.* 2014).

To evaluate the accuracy of the prediction we use the symmetric mean absolute percent error (SMAPE) and normalized root mean square deviation (NRMSD), defined in Eqn. (18). Both these measures are based on the difference between the porosity values (μ_l) extracted for a layer $l \; \forall \; l \in \{1 \dots L = 110\}$ from the offline CT scans and the predicted porosity values ($\widehat{\mu_l}$) for that layer obtained using the neural network.

$$SMAPE = \frac{1}{\mathrm{L}} \sum_{l=1}^{l=L} \frac{|\mu_l - \hat{\mu}_l|}{(|\mu_l| + |\hat{\mu}_l|)/2}; \;\; NRMSD = \frac{\sqrt{\sum_{l=1}^{l=L} (\mu_l - \hat{\mu}_l)^2}}{\sqrt{\sum_{l=1}^{l=L} \hat{\mu}_l}} \tag{18}$$

4 Results and Discussion

4.1 Porosity

The degree of porosity was found to vary as a function of processing conditions. Figure 8 shows a representative result before and after applying the pore extraction procedure described in Sec. 3.2. Measurements of the mean percentage of area covered by pores (ρ_1), the mean number of pores (ρ_2), the mean distance between pores (ρ_3), and the normalized porosity (μ) are provided in Table 2. The empirically observed frequency distribution (histogram, empirical probability mass function) of each porosity metric across each disc is also visualized in Figure 9. Disc D did not contain any pores and is not shown.

From Figure 9 and Table 2 it is apparent that Disc A has the most severe level of porosity; Disc A has the highest mean porosity proportion of pores per layer (ρ_1), highest mean number of pores per layer (ρ_2), smallest average distance between pores (ρ_3), and consequently, the largest mean normalized porosity level (μ). The samples in terms of descending level of pore severity are: Disc A, Disc B and Disc C, and Disc D.

Likewise, the empirically derived frequency distribution (histogram) of line-to-continuum ratio for 50,000 randomly selected data points from the same layer (layer 60) for the four discs A through D are overlaid in Figure 10(a), from which it is evident that there are clear differences in the distribution of the line-to-continuum ratios for the four discs, with the data from Disc A having an unusually large spread.

Further, the mean line-to-continuum ratio versus the layer number are shown in Figure 10(b), from which it is evident that there is a distinctive difference in the signal patterns for the four discs concerning their statistical characteristics, particularly, the mean line-to-continuum ratio is largely proportional to the input energy density. Nevertheless, as we will demonstrate herewith these statistical trends are not at par with graph theoretic features for capturing the layer-by-layer occurrence of porosity.

Table 2: The mean value of the three metrics ρ_1, ρ_2, and ρ_3 over 110 layers of the three discs extracted from their CT scans. The number in the parenthesis is the standard deviation.

Disc	ρ_1 Mean percentage of area covered by pores in each layer.	ρ_2 Mean number of pores in each layer (rounded)	ρ_3 Mean distance in pixels between pores in each layer	μ Mean normalized porosity measure in each layer.
Disc A	1.8% (0.828%)	102 (48)	223 (15.7)	0.64 (0.076)
Disc B	1.3% (0.997%)	78 (52)	233 (23.3)	0.57 (0.080)
Disc C	0.7% (0.810%)	40 (40)	263 (34.6)	0.57 (0.097)

Table 3 and Table 4 represent the classification accuracy of the predictions for two-level porosity and three-level porosity, respectively, in terms of F-score. The graph theory approach is compared therein with six different popular machine learning techniques using the principal components of the statistical features as inputs. We reiterate that the graph Fourier coefficients are used with a rudimentary KNN model. A summary of the model conditions used in these machine learning models are listed in Appendix II.

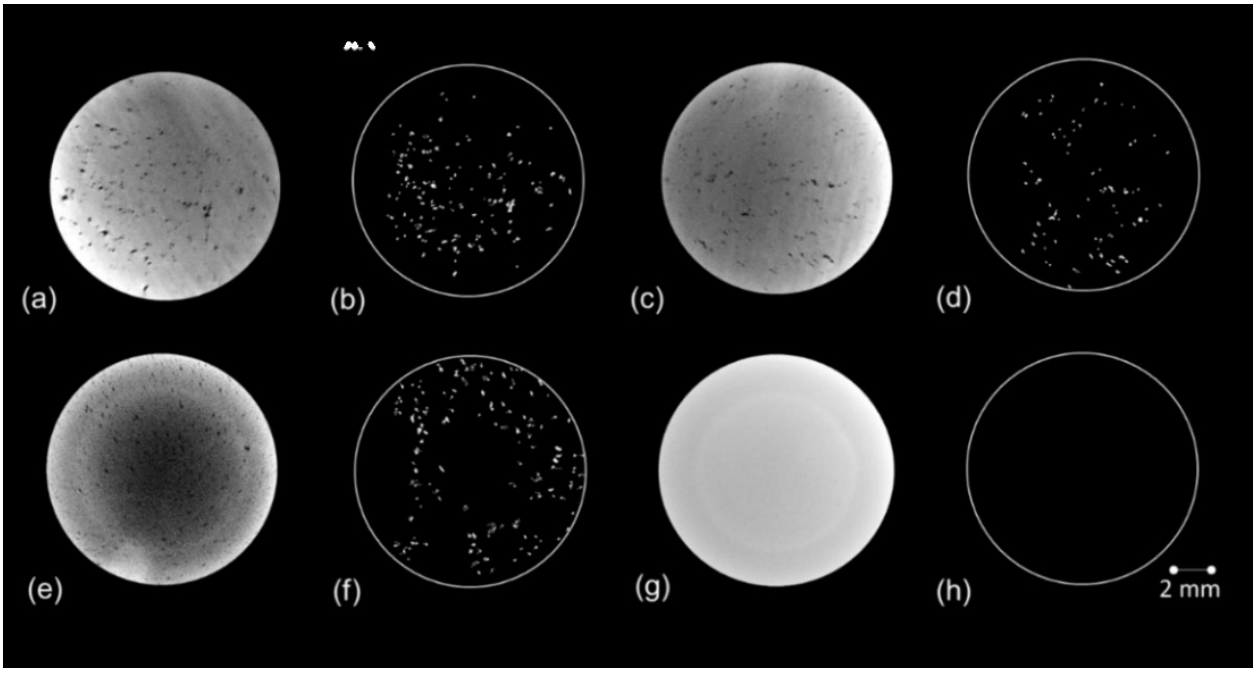

Figure 8: The pore extraction procedure is applied to the CT of layer 18 for Disc A through Disc D. The proportion of pores, their number, and spatial distribution are observed to vary across the discs.

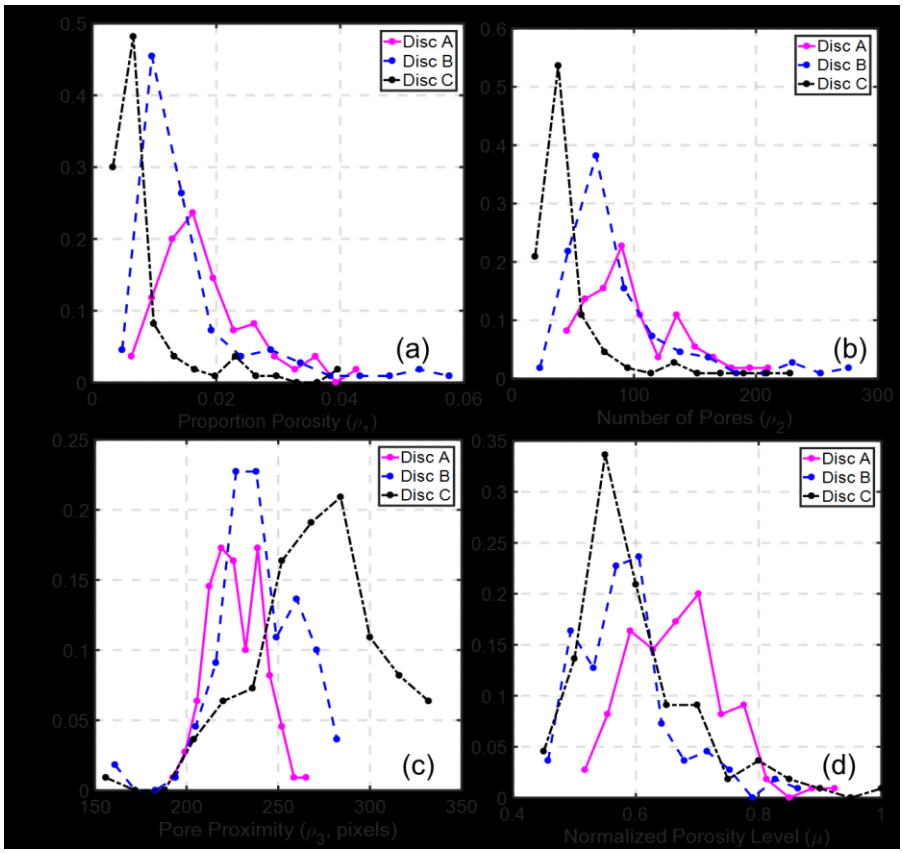

Figure 9: The three different porosity metrics (ρ_1, ρ_2, and ρ_3) shown in (a), (b), and (c) respectively. The normalized porosity level (μ) is charted in (d). In all these three metrics Disc A is observed to embody the most deletrious characteristics. Disc D is not represented because of the near-absolute absence of pores.

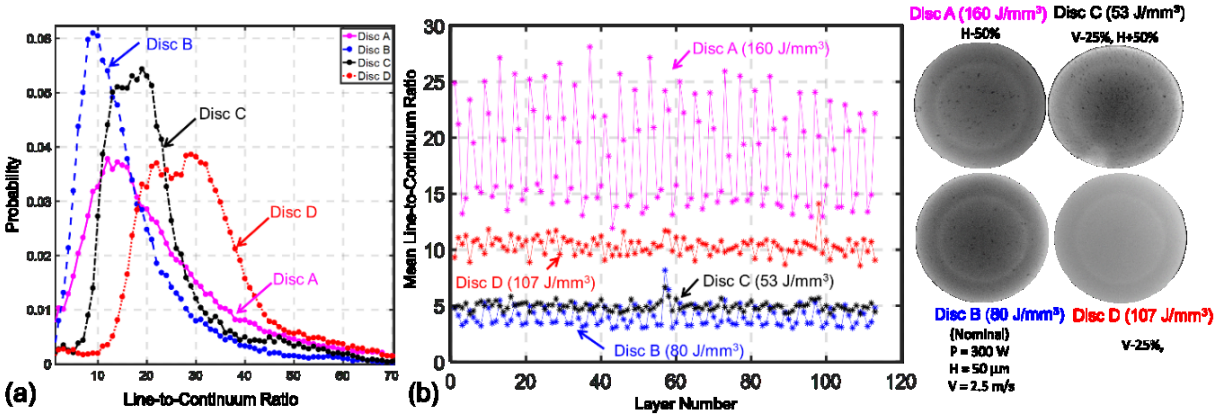

Figure 10(a): The frequency distribution (empirical probability mass function) of 50,000 randomly selected measurements of the line-to-continuum ratio for one layer (layer 60) of Disc A through D indicating the prominent differences in the signal characteristics. (b) The statistical mean of the line-to-continuum ratio charted layer-by-layer for the four Discs (A-D).

For the two-level classification case (Table 3(a)), the proposed method provides appreciably good results (F-score > 80%) with at least ~10% higher classification accuracy than other machine learning algorithms using all specified porosity measures ($\rho_1, \rho_2, \rho_3, and\ \mu$). From these results, it is evident that using he normalized porosity level (μ) as the output leads to higher F-score compared to the other metrics. For the three-level classification study, as reported in Table 4(a), the graph Fourier coefficients result in a classification accuracy approaching 80%, whereas with the statistical features the F-score is between 60% to 65%. The corresponding confusion matrices related to the two-level and three-level classification levels using the graph Fourier coefficients for the normalized porosity level (μ) are shown in Table 3(b) and Table 4(b), respectively. Notably, from the confusion matrix (Table 3(b)) for the two-level classification study, the Type II error (false negative) rate is only 1 in 287 layers across all disks. The type I errors (false positive) are higher – approximately 1 in 30 layers.

A possible reason for such a high-level of Type I error may be explained as follows. While a pore may be created in a layer, and promptly detected from the multispectral line-to-continuum emissions; subsequent layers are liable to re-melt lack-of-fusion pores in previous layers and thereby eliminate porosity. Both numerical simulations (Khairallah, Anderson *et al.* 2016, King, Anderson *et al.* 2015, King, Barth *et al.* 2014), and in-situ X-ray imaging (Leung, Marussi *et al.* 2018) demonstrate melting several layers below

the top surface. For the more challenging three-level classification, graph Fourier coefficient inputs also perform better than statistical features.

Table 3: Performance comparison for a two-level classification scenario using statistical features as inputs within six machine learning algorithms to a KNN using graph Fourier transform features as inputs. The numbers in the parenthesis are the standard deviations over a five-fold replication study.

(a) F-score results (as percentage) from classifying the porosity levels into two classes
$\rho_1 < 0.5\%$ as acceptable-level, $\rho_1 > 0.5\%$ as unacceptable-level porosity.
$\rho_2 < 30$ as acceptable-level, $\rho_2 > 30$ as unacceptable-level porosity.
$\rho_3 < 200$ as acceptable-level, $\rho_3 > 200$ as unacceptable-level porosity.
$\mu \leq 0.5$ as acceptable-level, $\mu > 0.5$ as unacceptable-level porosity.

Quantifier	Proposed Graph Theory Method	Machine learning Algorithm (Statistical features are used as inputs)					
		SVM	DT	KNN	LD	K-Means	NN
Proportion of area in a layer affected by porosity (ρ_1)	83 (1.4)	70 (0.4)	72 (1.4)	72 (1.1)	66 (0.5)	55 (19)	68 (2.5)
Frequency of occurrence, i.e., number of discrete pores in a layer (ρ_2)	82 (0.7)	67 (0.5)	70 (0.8)	69 (0.6)	64 (2.2)	55 (18)	66 (3.4)
Average distance between a pair of pores (ρ_3)	87 (1.0)	78 (0.6)	76 (0.2)	80 (0.5)	72 (0.7)	47 (7.7)	73 (2.3)
Normalized porosity (μ)	93 (1.1)	83 (0.8)	80 (0.3)	83 (1.0)	75 (0.6)	53 (12.8)	79 (3.4)

(b) Confusion matrix for classifying pore severity into two discrete levels using graph Fourier transform coefficients (Input Type 1) within a KNN model.

True Class ↓	Predicted Class	
	Acceptable Porosity $\mu < 0.5$	Unacceptable Porosity $\mu \geq 0.5$
Acceptable Porosity $\mu < 0.5$ (153 layers)	110 (out of 153)	43 (Type I error, False Alarm)
Unacceptable Porosity $\mu \geq 0.5$ (287 layers)	1 (Type II error, Failing to detect)	286 (out of 287)

Table 4: Performance comparison for a three-level classification scenario using statistical features as inputs within six machine learning algorithms to a KNN using graph Fourier transform features as inputs. The numbers in the parenthesis are the standard deviations for a five-fold replication study.

(a) F-score results (as percentage) from classifying the porosity levels into three classes

$\rho_1 \leq 0.5$ as low-level, $0.5 < \rho_1 \leq 1.2$ as medium-level, and $1.2 < \rho_1$ as high-level porosity.

$\rho_2 \leq 20$ as low-level, $20 < \rho_2 \leq 60$ as medium-level, and $60 < \rho_2$ as high-level porosity.

$\rho_3 \leq 200$ as low-level, $200 < \rho_3 \leq 240$ as medium-level, and $240 < \rho_3$ as high-level porosity.

$\mu = 0$ as low-level, $0 < \mu < 0.6$ as medium-level, and $0.6 \leq \mu$ as high-level porosity.

Quantifier	Proposed Graph Theory Method	Machine learning Algorithm (Statistical features are used as inputs)					
		SVM	DT	KNN	LD	K-Means	NN
Proportion of area in a layer affected by porosity (ρ_1)	68 (0.5)	53 (0.2)	59 (0.6)	60 (0.8)	54 (0.9)	32 (10.0)	65 (3.1)
Frequency of occurrence, i.e., number of discrete pores in a layer (ρ_2)	69 (1.3)	62 (0.8)	60 (1.0)	63 (0.7)	40 (0.5)	31 (9.0)	67 (2.1)
Average distance between a pair of pores (ρ_3)	74 (1.1)	67 (0.6)	63 (0.7)	66 (0.6)	50 (1.2)	28 (10.0)	69 (2.3)
Normalized porosity (μ)	79 (1.1)	63 (0.2)	65 (0.5)	62 (0.3)	55 (0.7)	31 (7.0)	70 (9.0)

(b) Confusion matrix for classifying pore severity into three discrete levels using graph Fourier transform coefficients (Input Type 1), and KNN.

True Class ↓	Predicted Class		
	Low-Level Porosity $\mu = 0$	Medium-Level Porosity $0 < \mu \leq 0.6$	High-Level Porosity $0.6 < \mu$
Low-Level Porosity $\mu = 0$ (110 layers)	109 (out of 110)	0	1
Medium-Level Porosity $0 < \mu < 0.6$ (196 layers)	1	165 (out of 196)	30
High-Level Porosity $0.6 \leq \mu$ (134 layers)	1	59	74 (out of 134)

Further evident from the confusion matrix for the three-level case shown in Table 4(b), with the graph Fourier coefficient inputs, 2 out of 330 cases – 1 in 196 layers belonging to the medium-level porosity class are grouped in the low porosity class, while 1 in 134 layers for the high-level porosity class are wrongly classified as belonging to the low-porosity level. On the other hand, there is a considerable degree of misclassification between the medium and high porosity levels. From the medium-level porosity, 30 layers (out of 196) are wrongly labeled as belonging to the high-level porosity class; conversely, 59 out of 134 layers belonging to the high-level class are misclassified within the medium-porosity level. The reason for the high-level of statistical errors in the three-level case compared to the two-level case is explained on the basis of the scatter plot shown in Figure 11, which shows the clustering efficacy of the first three principal components of the graph Fourier coeffecients with respect to the the normalized porosity metric (μ). The different levels of porosity are demarcated with different colors.

The principal components for the two-level case group into (two) distinct clusters, as evident in Figure 11(a), albeit, both Type I and Type II errors exist. In contrast, for the the three-level case, shown in Figure 11(b), only the low- and medium-level normalized porosity are tightly grouped, whereas the points representing layers belonging to the high-level porosity class have a large spread. The large spread in the input features, compounded with the effect of re-melting, is likely the root-cause for the high degree of misclassification evidenced in the three-level classification study.

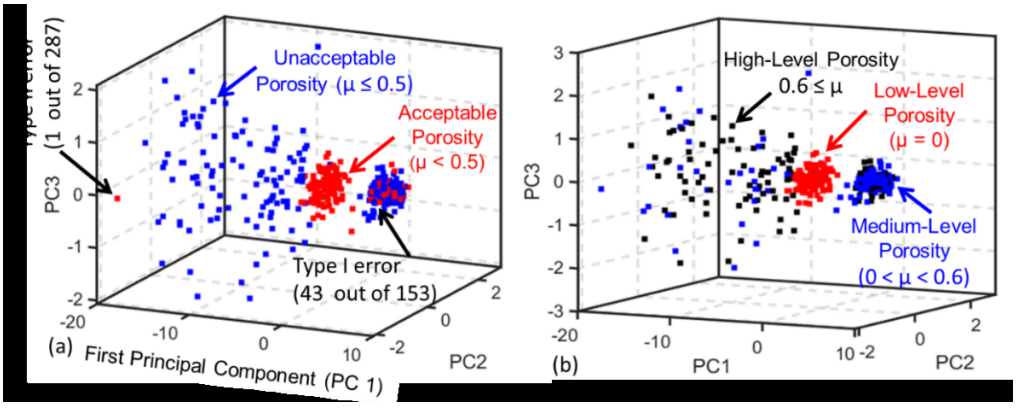

Figure 11: The scatter plot mapping the three principal components of the graph Fourier transform for the different levels of the normalized porosity metric (μ). (a) for the two-level case, the clusters are distinctive, (b) for the three-level case the principal components corresponding to the high-level of normalized porosity ($0.6 \leq \mu$) has a significant spread, which precludes clear demarcation.

In closing this section, a very pertinent concern expressed by one of the anonymous referees during the review process was *what level of accuracy would be necessary to satisfy certain quality level requirements in LPBF?* We recon the answer to this is question is contingent on three factors, namely, the application area where the AM part would be used, the location and criticality of the feature where a defect might occur, and whether the part is subjected to post-processing procedures, such as hot isostatic pressing, to negate the effect of porosity.

4.2 Estimating the Value of the Normalized Porosity Level (μ)

One concern with the confusion matrix is in the last row of Table 4(b), where 59 out of a total 134 layers that belong to the high-level porosity case are wrongly categorized as belonging to the medium-level porosity. An approach to overcome this limitation is to use a continuous threshold. This will also allow estimation of the exact porosity level. However, taking this approach entails sacrificing the tractability of rudimentary classification algorithms to a more sophisticated data modeling technique, such as a neural network. Using the graph Fourier coefficients as input features to a shallow feed-forward neural network with one hidden layer having 10 neurons (sigmoid activation function) the porosity-level is predicted in the output layer with a linear activation function.

Figure 12 shows both the observed porosity level (μ) overlaid with the values estimated ($\hat{\mu}$) obtained. Porosity is predicted with an error less than 15% for Disc A through Disc C. The prediction error for Disc D, which has a porosity level of zero ($\mu = 0$) is not estimated. The prediction accuracy is quantified in Table 5; Disc D is excluded due to the aforementioned reasons. Aggregating the predictions related to all discs, the normalized root-mean-square deviation (NRMSD) is less than 15%, and the symmetric mean absolute percentage (SMAPE) is roughly 11%.

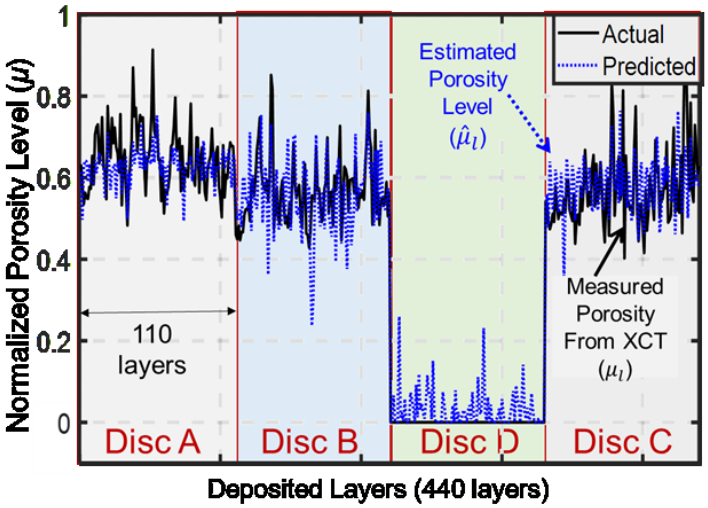

Figure 12: The actual vs predicted normalized porosity levels (μ) along the whole dataset using the graph Fourier coefficients (method 2).

Table 5: The goodness of fit in exact porosity prediction using a shallow neural network with graph Fourier coefficients as inputs.

Porosity Features	Prediction Error	
	SMAPE	NRMSD (%)
Disc A	0.09	0.11
Disc B	0.13	0.17
Disc C	0.12	0.16
Overall error	0.11	0.14

5 Conclusions and Future Work

In this work, we demonstrated a multispectral optical emission sensing technique and integrated it with a graph theoretic signal analysis technique for detection and identification of porosity in laser powder bed fusion (L-PBF) additive manufacturing of nickel alloy 718. The graph theoretic approach proposed in this work processes the line-to-continuum ratio from the multispectral sensor measurements on a layer-by-layer basis, and results in graph Fourier transform coefficients. We then test the hypothesis that the graph Fourier transform coefficients capture patterns that are symptomatic of the occurrence and severity of pores with higher statistical fidelity (F-score) compared to statistical features. Graph Fourier coefficients and statistical features are used as input to classify the severity of the porosity into discrete levels.

For two-level classification, the highest statistical fidelity (F-score > 90%) is obtained using graph Fourier coefficients. This is a ~10% higher classification accuracy, irrespective of the machine learning algorithm used, than with statistical input features. The computational time required for the approach is less than 0.5 second. For the three-level classification, the F-score degraded to 80% for Fourier coefficient inputs. This is a 15 to 20% improvement compared to statistical input features. The graph Fourier transform coefficients are also used for prediction of the porosity level, the prediction errors (normalized root-mean-square deviation, NMRSD) is approximately 10%.

In closure, this work demonstrates an approach to estimate porosity in real-time in an L-PBF process. Future work will investigate the effectiveness of the approach for different geometries, materials, and flaw types. This contribution is a step towards a qualify-as-you-build paradigm, wherein part quality is characterized from in-process sensor data, as opposed to post-process examination with X-Ray computed tomography.

Acknowledgements

The authors thank the three anonymous reviewers whose constructive comments and suggestions have doubtlessly improved the rigor of this work. The authors also thank the Associtate Editor of the Transactions, Professor Zhenyu Kong for shepherding this work through the review process.

Funding at Pennsylvania State University: This work was partially supported by the Office of Naval Research, under Contract No. N00014-11-1-0668. This work was also partially supported by the Air Force Research Laboratory through America Makes under agreement number FA8650-12-2-7230. Any opinions, findings and conclusions or recommendations expressed in this publication are those of the authors and do not necessarily reflect the views of the Office of Naval Research, Air Force Research Laboratory, or America Makes.

Funding at University of Nebraska-Lincoln: One of the authors (PKR) thanks the NSF for funding his research through the following grants CMMI-1719388, CMMI-1739696 and CMMI-1752069 (CAREER) at University of Nebraska-Lincoln. Specifically, the concept of using spectral graph theory for modeling in metal additive manufacturing applications was funded through CMMI-1752069 towards a *correct-as-you-build* smart additive manufacturing paradigm.

References

(2013). *Report to the National Institute of Standards and Technology: Measurement Science Roadmap for Metal-Based Additive Manufacturing*. Gaithersburg, MD, Energetics Corporation.

Abdelrahman, M., E. W. Reutzel, A. R. Nassar and T. L. Starr (2017). Flaw detection in powder bed fusion using optical imaging. *Additive Manufacturing* 15,1-11.

Calta, N. P., J. Wang, A. M. Kiss, A. A. Martin, P. J. Depond, G. M. Guss, V. Thampy, A. Y. Fong, J. N. Weker and K. H. Stone (2018). An instrument for in situ time-resolved X-ray imaging and diffraction of laser powder bed fusion additive manufacturing processes. *Review of Scientific Instruments* 89(5),055101.

Canny, J. (1987). A computational approach to edge detection. Readings in Computer Vision, Elsevier: 184-203.

Demuth, H. B., M. H. Beale, O. De Jesus and M. T. Hagan (2014). *Neural network design.* Boston, MA, PWS Publishing.

Dunbar, A. J. and A. R. Nassar (2018). Assessment of optical emission analysis for in-process monitoring of powder bed fusion additive manufacturing. *Virtual and Physical Prototyping* 13(1),14-19.

Everton, S. K., M. Hirsch, P. Stravroulakis, R. K. Leach and A. T. Clare (2016). Review of in-situ process monitoring and in-situ metrology for metal additive manufacturing. *Materials & Design* 95,431-445.

Foster, B. K., E. W. Reutzel, A. R. Nassar, C. J. Dickman and B. T. Hall (2015). A brief survey of sensing for additive manufacturing. SPIE Sensing Technology+ Applications, International Society for Optics and Photonics.

Gibson, I., D. W. Rosen and B. Stucker (2010). *Additive manufacturing technologies: rapid prototyping to direct digital manufacturing*, Springer.

Gobert, C., E. W. Reutzel, J. Petrich, A. R. Nassar and S. Phoha (2018). Application of supervised machine learning for defect detection during metallic powder bed fusion additive manufacturing using high resolution imaging. *Additive Manufacturing* 21,517-528.

Grasso, M. and B. M. Colosimo (2017). Process defects and in situ monitoring methods in metal powder bed fusion: a review. *Measurement Science and Technology* 28(4),044005.

Grasso, M., V. Laguzza, Q. Semeraro and B. M. Colosimo (2016). In-Process Monitoring of Selective Laser Melting: Spatial Detection of Defects Via Image Data Analysis. *Journal of Manufacturing Science and Engineering* 139(5),051001-051001-051016.

Huang, Y., M. C. Leu, J. Mazumder and A. Donmez (2015). Additive Manufacturing: Current State, Future Potential, Gaps and Needs, and Recommendations. *Transactions of the ASME, Journal of Manufacturing Science and Engineering* 137(1),014001.

Imani, F., A. Gaikwad, M. Montazeri and P. Rao (2018). Layerwise In-Process Quality Monitoring in Laser Powder Bed Fusion. ASME, Manufacturing Science and Engineering Conference. College Station, Texas, USA. Volume 1: Additive Manufacturing; Bio and Sustainable Manufacturing: V001T001A038-052.

Imani, F., A. Gaikwad, M. Montazeri, P. Rao, H. Yang and E. Reutzel (2018). Process Mapping and In-Process Monitoring of Porosity in Laser Powder Bed Fusion Using Layerwise Optical Imaging. *Journal of Manufacturing Science and Engineering* 140(10),101009-101009-101014.

Jacobsmuhlen, J. z., S. Kleszczynski, D. Schneider and G. Witt (2013). High resolution imaging for inspection of Laser Beam Melting systems. 2013 IEEE International Instrumentation and Measurement Technology Conference, IEEE.

Khairallah, S. A., A. T. Anderson, A. Rubenchik and W. E. King (2016). Laser powder-bed fusion additive manufacturing: physics of complex melt flow and formation mechanisms of pores, spatter, and denudation zones. *Acta Materialia* 108,36-45.

Khanzadeh, M., S. Chowdhury, L. Bian and M. A. Tschopp (2017). A methodology for predicting porosity from thermal imaging of melt pools in additive manufacturing thin wall sections. ASME 2017 12th international manufacturing science and engineering conference collocated with the JSME/ASME 2017 6th international conference on materials and processing, American Society of Mechanical Engineers.

Khanzadeh, M., S. Chowdhury, M. A. Tschopp, H. R. Doude, M. Marufuzzaman and L. Bian (2017). In-situ monitoring of melt pool images for porosity prediction in directed energy deposition processes. *IISE Transactions*,1-19.

King, W., A. Anderson, R. Ferencz, N. Hodge, C. Kamath, S. Khairallah and A. Rubenchik (2015). Laser powder bed fusion additive manufacturing of metals; physics, computational, and materials challenges. *Applied Physics Reviews* 2(4),041304.

King, W. E., H. D. Barth, V. M. Castillo, G. F. Gallegos, J. W. Gibbs, D. E. Hahn, C. Kamath and A. M. Rubenchik (2014). Observation of keyhole-mode laser melting in laser powder-bed fusion additive manufacturing. *Journal of Materials Processing Technology* 214(12),2915-2925.

Kramida, A., Y. Ralchenko and J. Reader (2017). NIST Atomic Spectra Database Gaithersburg, MD, National Institute of Standards and Technology (NIST).

Krauss, H., C. Eschey and M. Zaeh (2012). Thermography for monitoring the selective laser melting process. Proceedings of the Solid Freeform Fabiraction Conference, Austin, TX.

Lane, B., B. Lane, S. Moylan, S. Moylan, E. P. Whitenton, E. P. Whitenton, L. Ma and L. Ma (2016). Thermographic measurements of the commercial laser powder bed fusion process at NIST. *Rapid prototyping journal* 22(5),778-787.

Lane, B., E. Whitenton and S. Moylan (2016). Multiple sensor detection of process phenomena in laser powder bed fusion. SPIE Commercial+ Scientific Sensing and Imaging, International Society for Optics and Photonics.

Leung, C. L. A., S. Marussi, R. C. Atwood, M. Towrie, P. J. Withers and P. D. Lee (2018). In situ X-ray imaging of defect and molten pool dynamics in laser additive manufacturing. *Nature Communications* 9(1),1355.

Lewandowski, J. J. and M. Seifi (2016). Metal additive manufacturing: a review of mechanical properties. *Annual Review of Materials Research* 46,151-186.

Mahmoudi, M., A. A. Ezzat and A. Elwany (2019). Layerwise Anomaly Detection in Laser Powder-Bed Fusion Metal Additive Manufacturing. *Journal of Manufacturing Science and Engineering* 141(3),031002-031002-031013.

Mani, M., B. M. Lane, M. A. Donmez, S. C. Feng and S. P. Moylan (2017). A review on measurement science needs for real-time control of additive manufacturing metal powder bed fusion processes. *International Journal of Production Research* 55(5),1400-1418.

Maskery, I., N. T. Aboulkhair, M. R. Corfield, C. Tuck, A. T. Clare, R. K. Leach, R. D. Wildman, I. A. Ashcroft and R. J. M. Hague (2016). Quantification and characterisation of porosity in

selectively laser melted Al–Si10–Mg using X-ray computed tomography. *Materials Characterization* 111,193-204.

Mazumder, J. (2015). Design for Metallic Additive Manufacturing Machine with Capability for "Certify as You Build". *Procedia CIRP* 36,187-192.

Mazumder, J., D. Dutta, N. Kikuchi and A. Ghosh (2000). Closed loop direct metal deposition: art to part. *Optics and Lasers in Engineering* 34(4),397-414.

Mazumder, J. and L. Song (2016). Smart additive manufacturing system USPTO.

Mazumder, J., L. Song and C. Wang (2017). In-situ identification and control of microstructures produced by phase transformation of a material. USPTO. United States, University of Michigan.

Mies, D., W. Marsden, S. Dyer and S. Warde (2016). Data-driven certification of additively manufactured parts. Proceedings of 57th AIAA/ASCE/AHSIASC Structures, Structural Dynamics, and Materials Conference.

Montazeri, M. and P. Rao (2018). Sensor-Based Build Condition Monitoring in Laser Powder Bed Fusion Additive Manufacturing Process Using a Spectral Graph Theoretic Approach. *Journal of Manufacturing Science and Engineering* 140(9),091002-091002-091016.

Montazeri, M., R. Yavari, P. Rao and P. Boulware (2018). In-Process Monitoring of Material Cross-Contamination Defects in Laser Powder Bed Fusion. *ASME Transactions, Journal of Manufacturing Science and Engineering* 140(11),111001-111019.

Nassar, A., T. Spurgeon and E. Reutzel (2014). Sensing defects during directed-energy additive manufacturing of metal parts using optical emissions spectroscopy. Solid Freeform Fabrication Symposium, University of Texas, Austin, TX.

Nassar, A., B. Starr and E. Reutzel (2015). Process monitoring of directed-energy deposition of Inconel-718 via plume imaging. Solid Freeform Fabrication Symposium, Austin, TX.

Olakanmi, E. O., R. F. Cochrane and K. W. Dalgarno (2015). A review on selective laser sintering/melting (SLS/SLM) of aluminium alloy powders: Processing, microstructure, and properties. *Progress in Materials Science* 74,401-477.

Peralta, A. D., M. Enright, M. Megahed, J. Gong, M. Roybal and J. Craig (2016). Towards rapid qualification of powder-bed laser additively manufactured parts. *Integrating Materials and Manufacturing Innovation*,1-23.

Rao, P. K., O. F. Beyca, Z. Kong, S. T. S. Bukkapatnam, K. E. Case and R. Komanduri (2015). A graph-theoretic approach for quantification of surface morphology variation and its application to chemical mechanical planarization process. *IIE Transactions* 47(10),1088-1111.

Repossini, G., V. Laguzza, M. Grasso and B. M. Colosimo (2017). On the use of spatter signature for in-situ monitoring of Laser Powder Bed Fusion. *Additive Manufacturing* 16,35-48.

Sames, W. J., F. List, S. Pannala, R. R. Dehoff and S. S. Babu (2016). The metallurgy and processing science of metal additive manufacturing. *International Materials Reviews* 61(5),315-360.

Sandryhaila, A. and J. M. Moura (2013). Discrete signal processing on graphs. *IEEE Transactions on Signal Processing* 61,1644-1656.

Seifi, M., M. Gorelik, J. Waller, N. Hrabe, N. Shamsaei, S. Daniewicz and J. J. Lewandowski (2017). Progress Towards Metal Additive Manufacturing Standardization to Support Qualification and Certification. *JOM* 69(3),439-455.

Sharrat, B. (2015). Literature review: Non-Destructive Techniques and Technologies for Qualification of Additive Manufactured Parts and Processes. Victoria, BC, Canada Defence Research and Development Institute. DRDC-RDDC-2015-C035.

Shuman, D. I., S. K. Narang, P. Frossard, A. Ortega and P. Vandergheynst (2013). The emerging field of signal processing on graphs: Extending high-dimensional data analysis to networks and other irregular domains. *IEEE Signal Processing Magazine* 30(3),83-98.

Shuman, D. I., B. Ricaud and P. Vandergheynst (2012). A windowed graph Fourier transform. 2012 IEEE Statistical Signal Processing Workshop (SSP), Ieee.

Slotwinski, J. A., E. J. Garboczi and K. M. Hebenstreit (2014). Porosity Measurements and Analysis for Metal Additive Manufacturing Process Control. *Journal of research of the National Institute of Standards and Technology* 119,494-528.

Smith, R. J., W. Li, J. Coulson, M. Clark, M. G. Somekh and S. D. Sharples (2014). Spatially resolved acoustic spectroscopy for rapid imaging of material microstructure and grain orientation. *Measurement Science and Technology* 25(5),055902.

Song, L., V. Bagavath-Singh, B. Dutta and J. Mazumder (2012). Control of melt pool temperature and deposition height during direct metal deposition process. *The International Journal of Advanced Manufacturing Technology* 58(1),247-256.

Song, L. and J. Mazumder (2011). Feedback Control of Melt Pool Temperature During Laser Cladding Process. *IEEE Transactions on Control Systems Technology* 19(6),1349-1356.

Song, L. and J. Mazumder (2015). Real-time implementation of generalized predictive algorithm for direct metal deposition (DMD) process control, DM3D Tech, LLC.

Spears, T. G. and S. A. Gold (2016). In-process sensing in selective laser melting (SLM) additive manufacturing. *Integrating Materials and Manufacturing Innovation* 5(1),2.

Spierings, A. B., M. Schneider and R. Eggenberger (2011). Comparison of density measurement techniques for additive manufactured metallic parts. *Rapid Prototyping Journal* 17(5),380-386.

Stutzman, C. B., A. R. Nassar and E. W. Reutzel (2018). Multi-sensor investigations of optical emissions and their relations to directed energy deposition processes and quality. *Additive Manufacturing* 21,333-339.

Tapia, G. and A. Elwany (2014). A Review on Process Monitoring and Control in Metal-Based Additive Manufacturing. *Transactions of the ASME, Journal of Manufacturing Science and Engineering* 136(6),060801.

Tapia, G., A. Elwany and H. Sang (2016). Prediction of porosity in metal-based additive manufacturing using spatial Gaussian process models. *Additive Manufacturing* 12,282-290.

Tootooni, M. S., C. Liu, D. Roberson, R. Donovan, P. K. Rao, Z. Kong and S. T. S. Bukkapatnam (2016). Online non-contact surface finish measurement in machining using graph theory-based image analysis. *Journal of Manufacturing Systems* 41,266-276.

Tootooni, M. S., P. K. Rao, C.-A. Chou and Z. J. Kong (2018). A Spectral Graph Theoretic Approach for Monitoring Multivariate Time Series Data from Complex Dynamical Processes. *IEEE Transactions Automation Science and Engineering* 15(1),127-144.

Williams, J., P. Dryburgh, A. Clare, P. Rao and A. Samal (2018). Defect Detection and Monitoring in Metal Additive Manufactured Parts through Deep Learning of Spatially Resolved Acoustic Spectroscopy Signals. *Smart and Sustainable Manufacturing Systems* 2(1)

Yadollahi, A., M. J. Mahtabi, A. Khalili, H. R. Doude and J. C. Newman (2018). Fatigue life prediction of additively manufactured material: Effects of surface roughness, defect size, and shape. *Fatigue & Fracture of Engineering Materials & Structures* 41(7),1602-1614.

Yavari, M. R., K. D. Cole and P. Rao (2019). Thermal Modeling in Metal Additive Manufacturing Using Graph Theory. *Journal of Manufacturing Science and Engineering* 141(7),071007-071007-071020.

Yusuf, S. M. and N. Gao (2017). Influence of energy density on metallurgy and properties in metal additive manufacturing. *Materials Science and Technology* 33(11),1269-1289.

Appendix I

The following table represents the classification accuracy (F-score) of the 2 and 3-level classification using a KNN with different signal lengths.

Signal window length (number of line-to-continuum data points per layer)	2-level classification Percentage F-score	3-level classification Percentage F-score
20	78%	71%
50 (chosen for analysis)	93%	79%
100	80%	71%
200	78%	71%
400	76%	70%

Appendix II

Type	Setting
Support Vector Machine (SVM)	• Kernel Function: Linear • Box constraint level: 1
Decision Tree (DT)	• Max. No. of splits: 20 • Split Criterion: Gini's diversity Index
K-Nearest Neighbor (KNN)	• No. of Neighbors: 10 • Distance Metric: Euclidean
Neural Network (NN)	• No. of Layers: 2 • No. of Hidden Neurons: 10 • Training method: Scaled conjugate gradient backpropagation
Linear Discriminant (LD)	• Kernel Function: Linear
K-Means Clustering	• No. of Clusters: 2 and 3

Author Biographies

Mohammad Montazeri is a PhD candidate in Engineering at University of Nebraska-Lincoln, under the supervision Dr. Prahalada Rao, and is set to graduate in Fall of 2018. He has over 8 years of industrial engineering-related expertise in different industries, ranging from insurance, automotive, IT, and nanotechnology. His expertise is in data analytics with a strong background in statistical analysis along with vast experience in implementing machine learning algorithms and predictive modeling in the additive manufacturing area.

Dr. Abdalla R. Nassar is an Associate Research Professor and the acting head of the Process Physics, Analytics, and Engineering Department within the Materials Science Division of the Applied Research Laboratory (ARL) at Penn State. He earned his B.S and Ph.D. in Engineering Science and Mechanics from the Pennsylvania State University in 2008 and 2012, respectively. Dr. Nassar has been with ARL since 2013 and has severed as principle investor and participated in numerous programs on laser processing, powder bed fusion, and directed energy additive manufacturing (AM). Dr. Nassar also has Graduate Faculty appointments with the Engineering Science and Mechanics Department and the Additive Manufacturing & Design Graduate Program at Penn State. He has developed and taught graduate-level courses on laser-material interactions and the scientific foundations of additive manufacturing. He has also instructed several industrial practicums and technology exchanges related to additive manufacturing. His work has led to six patent filings along with numerous publications on topics including the digital thread concept for AM, sensing and control of AM processes, defect detection, post-processing methods for support removal,

modeling AM processes, laser-plasma nitriding of titanium, and characterization of plasma via optical emission spectroscopy.

Dr Alexander J. Dunbar is an active researcher in the field of additive manufacturing currently working in the private sector. He earned his B.S. in 2011 from Bucknell and his Ph.D from The Pennsylvania State University in 2016, both in the field of Mechanical Engineering. He has experience designing sub-systems for additive manufacturing machines for both production and experiments. In the past, he has developed high-level sensing systems to aid in experimental measurement of the powder bed fusion process. His current work includes process development and improvement of in situ build quality assessment techniques for additive manufacturing.

Prahalada Rao is currently an Assistant Professor in the Mechanical and Materials Engineering Department, University of Nebraska-Lincoln. His scholastic passion is encapsulated in three words manufacturing, sensing, and analytics. His research on modeling and sensor-based monitoring of complex physical and natural systems has garnered funding exceeding $1 million by the National Science Foundation (NSF), including the 2018 NSF CAREER award for sensor-based monitoring and control of additive manufacturing processes. He was awarded the 2017 Society of Manufacturing Engineers, Yoram Koren Outstanding Young Manufacturing Engineer Award; 2017 IISE Best Paper Award (Honorable Mention); 2018 IISE Transactions Best Paper Award; 2018 Outstanding Reviewer Award from the Society of Manufacturing Engineers; 2019 University of Nebraska-Lincoln (UNL), College of Engineering Research and Creativity Award. He has published over 35 papers in advanced manufacturing, including ultraprecision diamond turning and semiconductor manufacturing. Dr. Rao currently organizes special sessions concerning sensing and quality assurance in Additive Manufacturing at two flagship conferences, namely, The American Society of Mechanical Engineers, Manufacturing Science and Engineering Conference, and the Solid Freeform Fabrication Conference. At UNL he currently teaches courses in Additive Manufacturing, Statistics, and Quality Control. He is a certified amateur radio operator with the call sign K5RAO.